Supplementary Information

Defect-rich heterostructures Co-$MoS_{2-x}O_x$@NC fibers derived from in-situ grown metal-organic frameworks towards high electromagnetic wave absorption

Keru Song, Anze Shui*, Hulei Yu*

School of Materials Science and Engineering, South China University of Technology, Guangzhou 510641, China

E-mail: shuianze@scut.edu.cn; huleiyu@scut.edu.cn

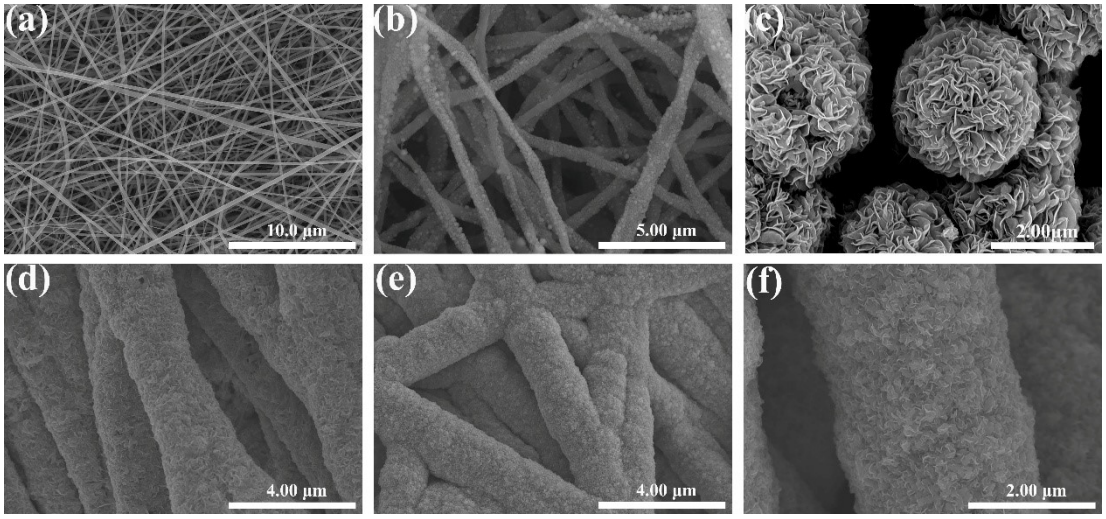

Fig.S1 SEM images of (a) CNF, (b) Co@NC, (c) O-MoS_2, (d) O-MoS_2@ZIF-67@PAN, (e) CMN-700, and (f) further enlargement of the image.

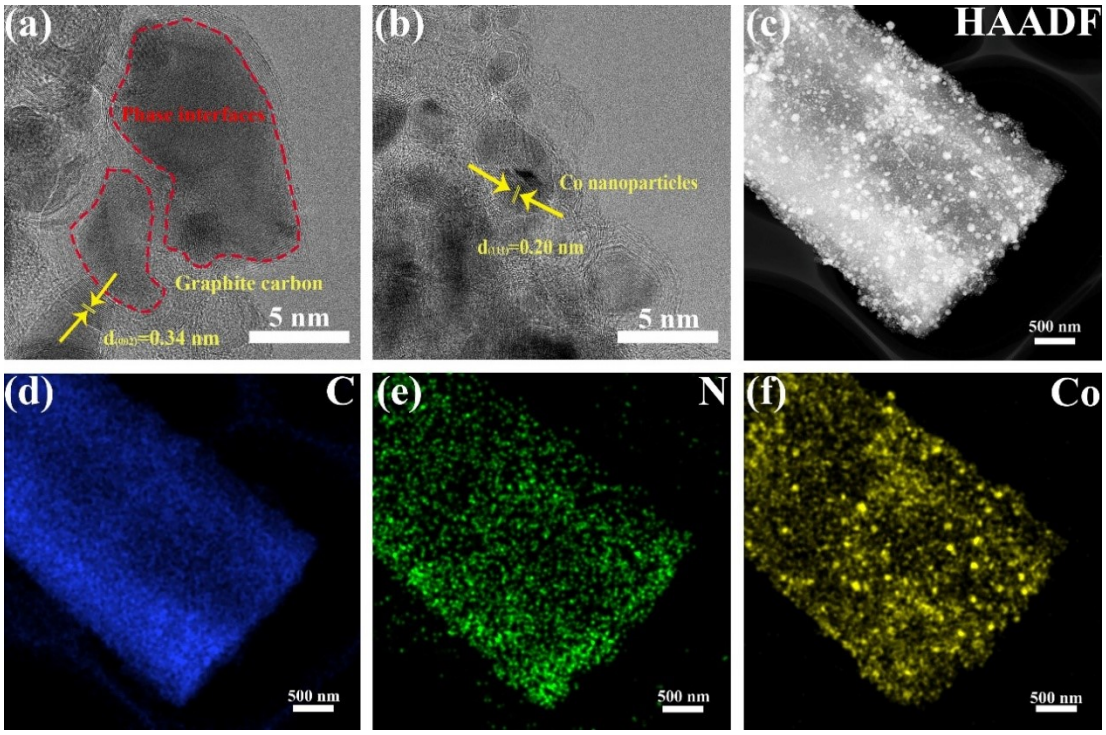

Fig. S2 TEM image of (a, b) Co@NC fiber, (c) HAADF, and (d-f) EDS results.

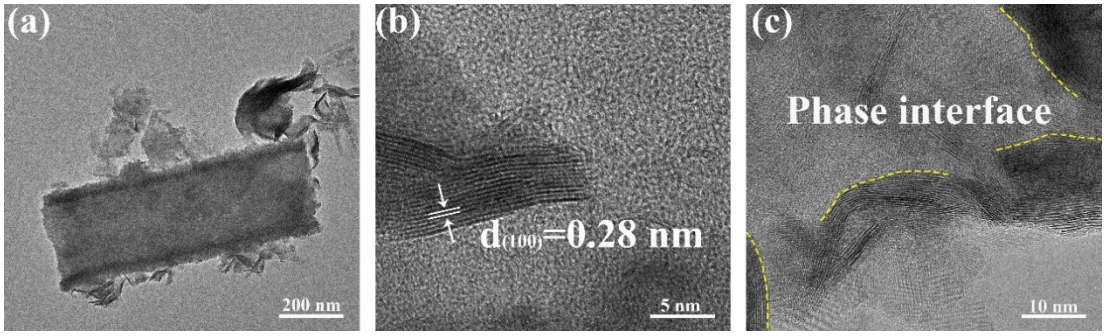

Fig. S3 TEM images of CMN-700 obtained in Ar atmosphere.

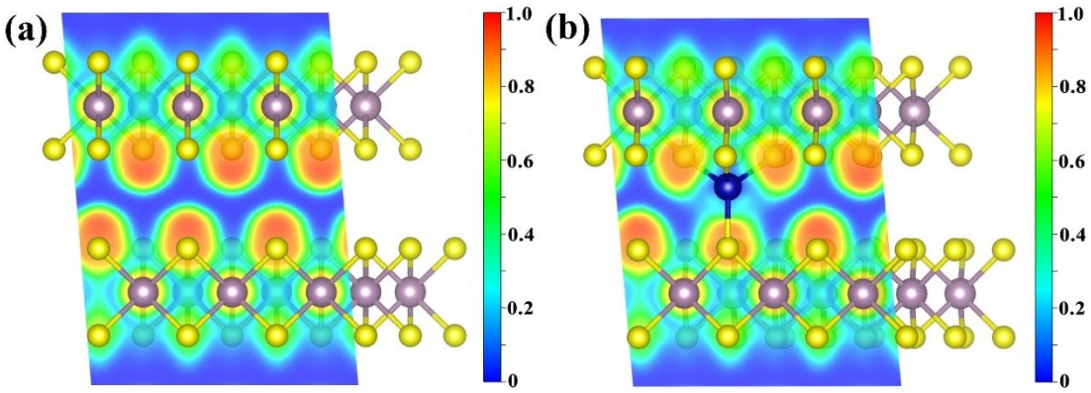

Fig. S4 The electronic location function of (a) MoS_2, (b) Co-MoS_2.

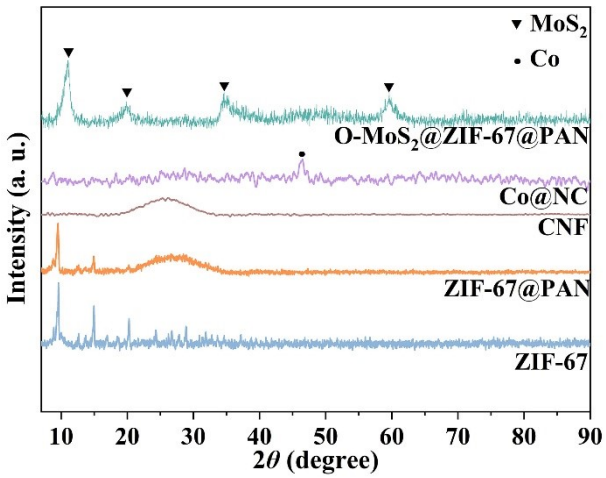

Fig. S5 XRD spectrum of ZIF-67, ZIF-67@PAN, CNF, Co@NC, and O-MoS_2@ZIF-67@PAN.

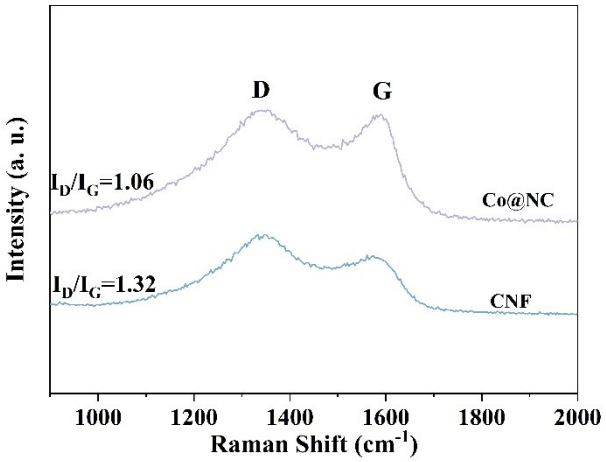

Fig. S6 Raman spectrum of CNF and Co@NC.

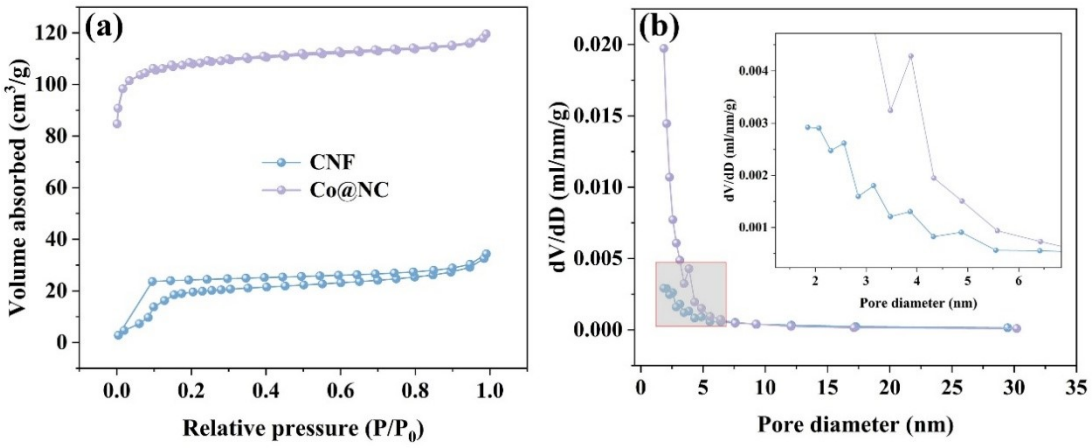

Fig. S7 N_2 adsorption-desorption isotherms and pore size distributions of CNF and Co@NC fibers.

Table S1 Pore structure parameters of nanofiber composite materials.

Sample	BET surface area (m^2/g)	Pore volume (cm^3/g)	Average pore size (nm)
CNF	42.76	0.05	4.94
Co@NC	424.51	0.18	1.74
CMN-600	185.88	0.12	2.60
CMN-700	209.16	0.14	2.66
CMN-800	135.26	0.11	3.19

Table S2: Volume fractions of CNF, Co, Co-$MoS_{2-x}O_x$, and porosity in CNF, Co@NC, and CMN composites.

Sample	CNF (vol%)	Co (vol%)	Co-$MoS_{2-x}O_x$ (vol%)	Porosity (vol%)
CNF	49.82	-	-	50.18
Co@NC	32.66	1.30	-.	66.04
CMN-600	33.19	-	17.09	49.72
CMN-700	31.77		16.70	51.53
CMN-800	31.10	-	18.95	49.95

Systematic calculations indicate that the Co@NC sample exhibits the highest porosity, consistent with the maximum specific surface area results obtained via N_2 adsorption-desorption isotherms. This is primarily attributed to the fact that the pyrolysis of ZIF-67 itself generates a vast number of micropores, while the Co nanoparticles encapsulated within the carbon matrix do not significantly obstruct these pores. ICP results indicate the mass fraction of Co is 12.54%, but its extremely high density results in it occupying only approximately 1.3 vol% within the composite material. Therefore, the introduction of a small amount of Co can significantly alter the electromagnetic properties without compromising the porous structure. This structure demonstrates that the ZIF-67 derived strategy successfully constructed a composite structure with high-porosity carbon as the continuous phase, in which low volume fraction magnetic Co nanoparticles are highly dispersed, laying the foundation for subsequent composite formation with MoS_2. The CMN-700 sample exhibits favorable porosity (51.53 vol%), indicating the formation of a rich and stable nanoporous structure at this temperature. This structure originates from the complete carbonization of the precursor and the thorough escape of gases, while the robust carbon framework effectively resists pore collapse during the pressing process. When the temperature rises to 800 °C, the porosity decreases to 49.90 vol%. The reduction is attributed to the coarsening and coalescence of pore structures caused by high temperatures, along with partial ablation of the carbon skeleton. This process makes the pores more susceptible

to deformation and densification under pressure, consistent with the observed minimum specific surface area results. The 600 °C sample exhibited insufficient framework strength due to incomplete carbonization, resulting in a porosity (49.72 vol%) that did not reach the optimal level.

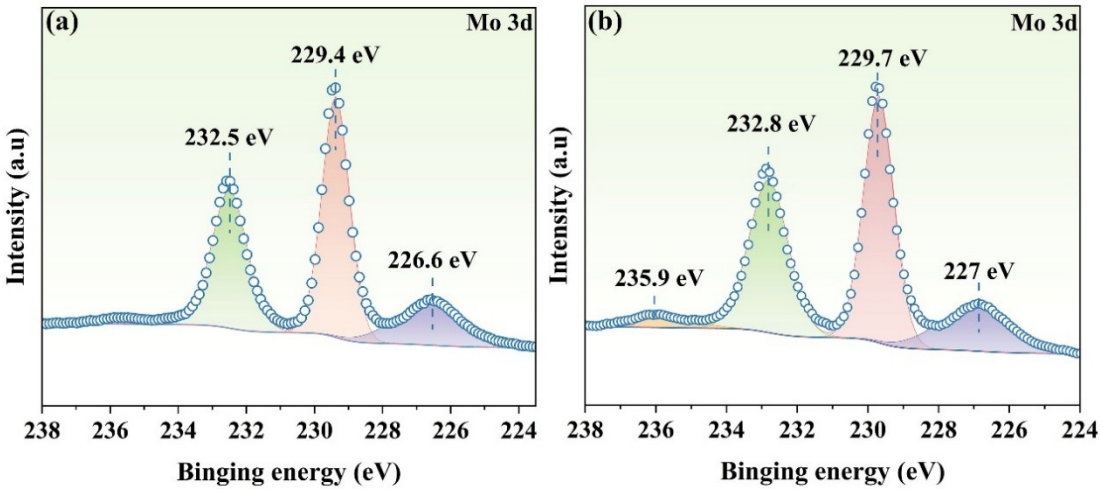

Fig. S8 Mo 3d spectrum of (a) MoS_2, (b) O-MoS_2.

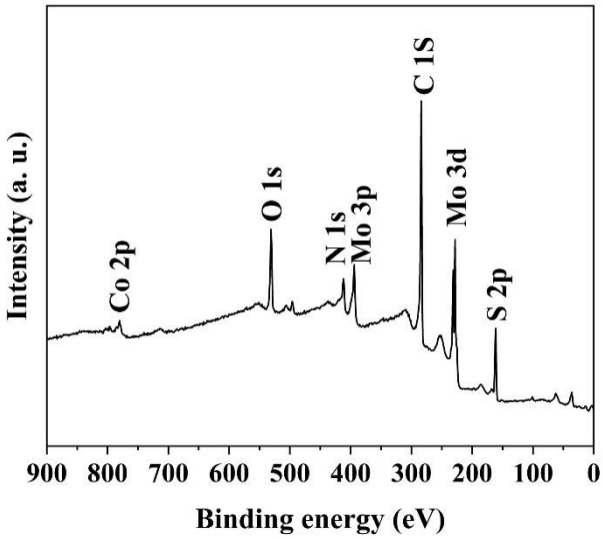

Fig. S9 XPS full spectrum of the CMN-700 sample.

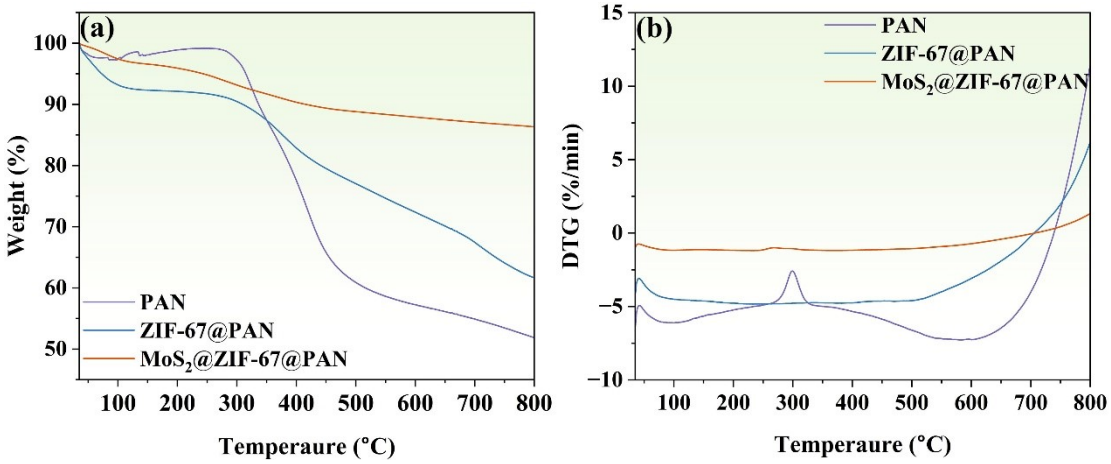

Fig. S10 (a) TG and (b) DSC curve of CNF, ZIF-67@PAN, and O-MoS_2@ZIF-67@PAN with heat treatment under argon.

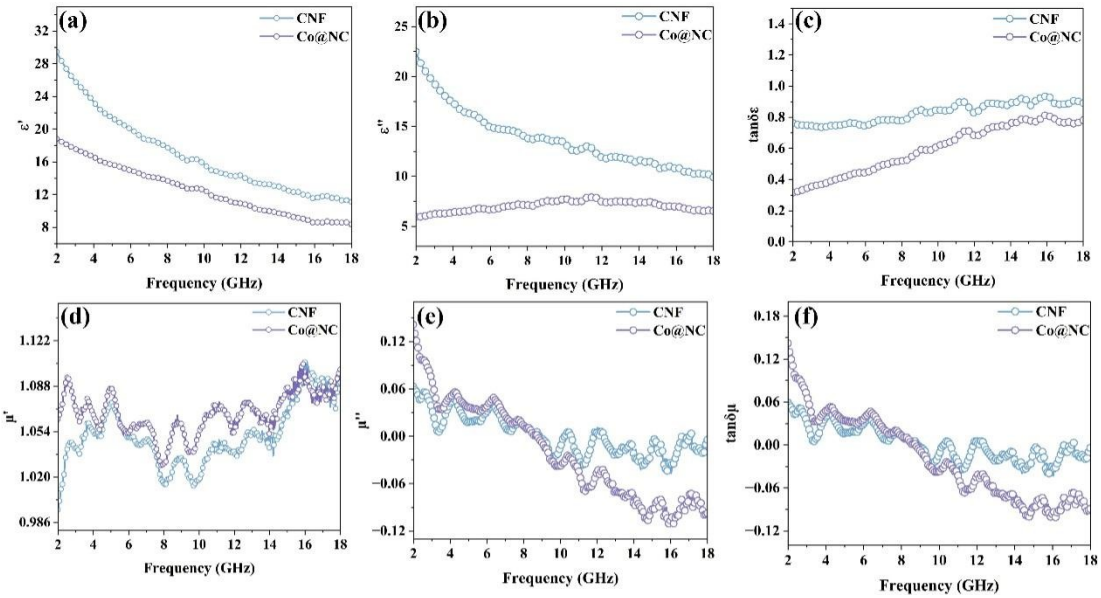

Fig. S11(a) Real part, (b) imaginary part of complex permittivity, (c) dielectric loss tangent, (d) real part, (e) imaginary part of complex permeability, and (f) magnetic loss tangent of CNF and Co@CN sample.

To investigate the influence of the shell-core structure on EMW absorption performance, Fig. S11(a-c) presents the dielectric properties of CNF and Co@NC. Pristine CNF exhibits a higher dielectric constant, which may lead to surface current concentration and thereby induce the skin effect, ultimately resulting in impedance mismatch. Consequently, incident EMWs are largely reflected as much as possible instead of penetrating the surface. In contrast, the Co@NC sample demonstrates a slightly reduced dielectric constant, which can be attributed to the increased defect density resulting from ZIF-67 pyrolysis. This enhancement improves impedance matching and simultaneously promotes magnetic loss. As shown in Fig. S11(d-e), all samples display distinct fluctuations in dielectric behavior across the 2-18 GHz range, which are associated with the irregular polarization and charge migration within the magnetic components.

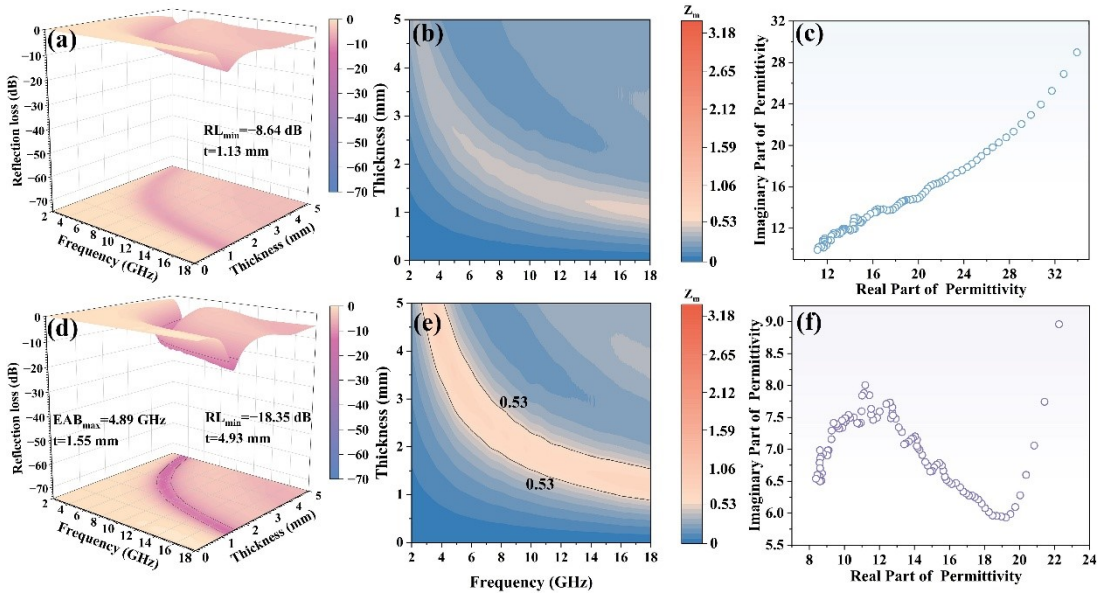

Fig. S12 3D RL diagrams, impedance matching degree dependence of the frequency, and Cole-Cole curves of (a-c) CNF, (d-f) Co@NC.

A comparison of the curves presented in Fig. S12(c) and S12(f) reveals that the tail region of the ε'-ε'' curve for CNF exhibits a distinct linear trend, indicative of conductivity-related loss. In contrast, the Co@NC composite nanofibers display multiple semicircular features, which suggest the presence of several polarization relaxation mechanisms. Material defects can result in asymmetric charge distribution, thereby promoting dipole polarization. Furthermore, significant interfacial polarization loss is observed at the Co@NC fiber interface, attributable to charge accumulation at this boundary. Due to the high electrical conductivity of CNF, impedance mismatch arises, resulting in poor electromagnetic wave absorption performance (Fig. S12(b)). At a thickness of 1.13 mm, the RL_{min} reaches only -8.64 dB (Fig. S12(a)). In comparison, Co@NC exhibits an EAB_{max} of 4.89 GHz at a reduced thickness of 1.55 mm, while achieving a minimum reflection loss of -18.35 dB at 4.93 mm (Fig. S12(d, e)).

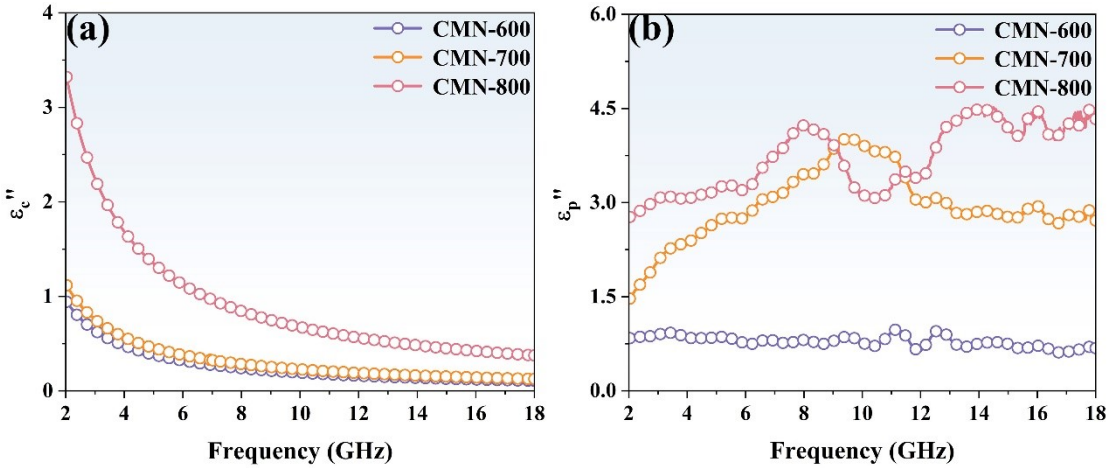

Fig.S13 (a) Conduction loss and (b) polarization loss of CMN absorbers.

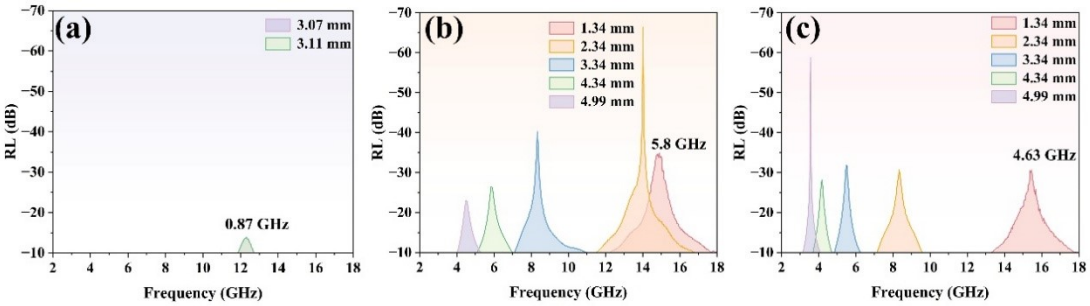

Fig.S14 2D EAB map of (a) CMN-600, (b) CMN-700, and (c) CMN-800.

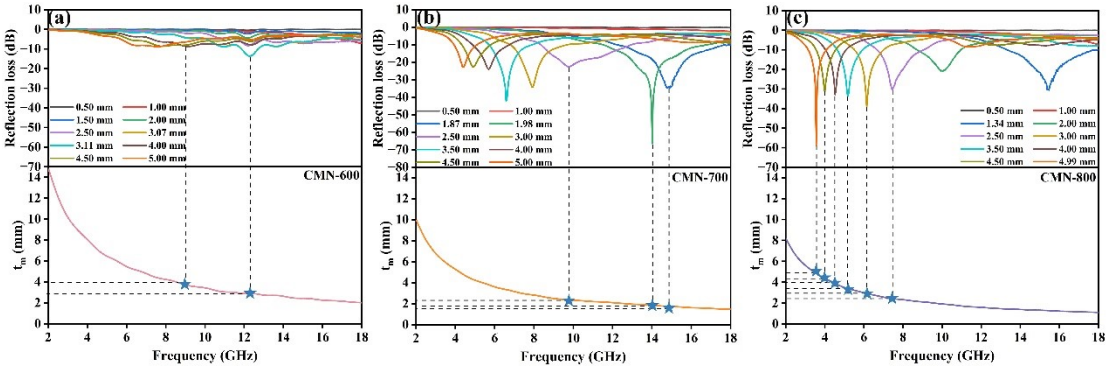

Fig. S15 2D RL curves and equally matched thickness curves of (a) CMN-600, (b) CMN-700, and (c) CMN-800.

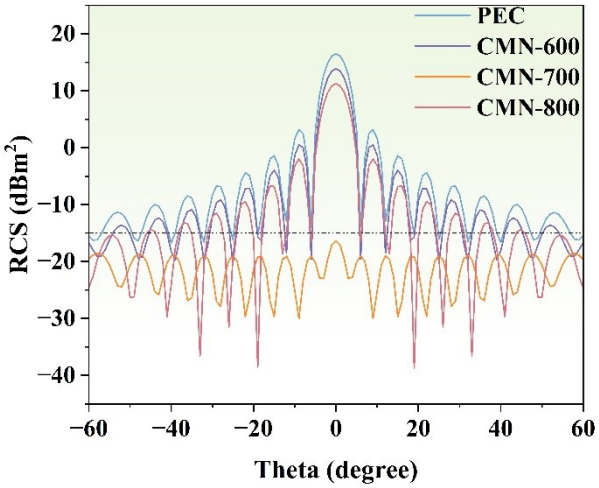

Fig. S16 RCS simulation curves for PEC and its various CMN absorber coatings.

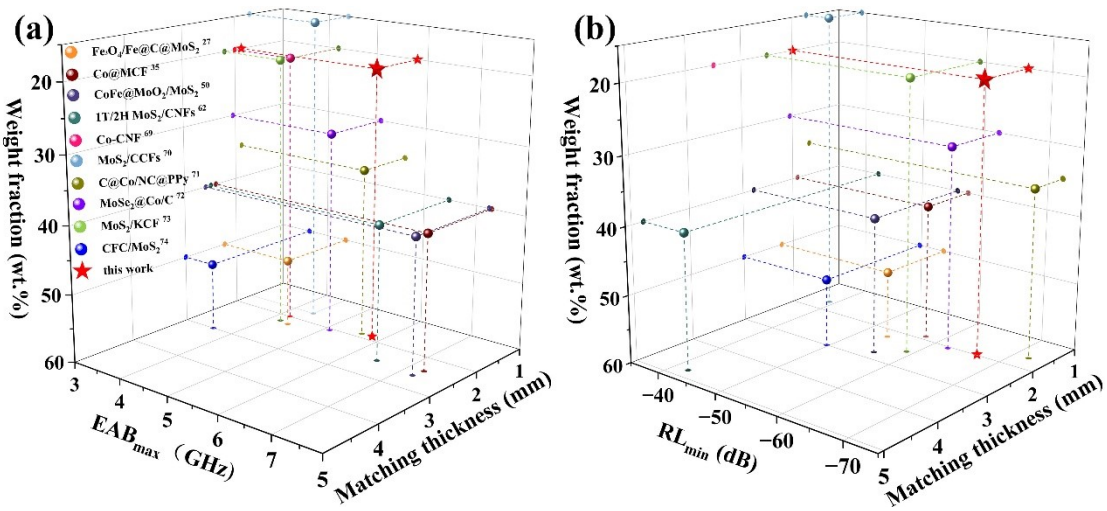

Fig. S17 The comparison of absorption performance with relevant absorbers.